Chapter 5
Noise Spectral Density of Hysteretic Systems

5.1 Spectral Density of Bistable Hysteretic Systems with Diffusion Input

In this section, closed form expressions for the spectral densities of bistable hysteretic systems driven by diffusion inputs are found by analytical means using the theory of stochastic processes on graphs. In the particular case of Ornstein-Uhlenbeck (OU) input, the output spectra are explicitly computed and analyzed, discussing the influence of input drift and diffusion coefficients, as well as of the rectangular loop width on the output spectra characteristics. The spectrum of bistable hysteretic system driven by colored noise is analyzed by numerical means using the Monte-Carlo method presented in Chap. 2. Since complex hysteretic nonlinearities with stochastic input can be described through Preisach formalism as weighted superposition of stochastically driven rectangular loop operators, this analysis is also useful for better understanding of spectra in complex hysteretic systems discussed in the next sections.

5.1.1 Statement of the Problem

Consider the bistable system with hysteresis represented in Fig. 5.1 that can be mathematically described by the following input–output relation:

$$I_{\beta\alpha}(t) = \hat{\gamma}_{\beta\alpha}X(t) = \begin{cases} 1, \text{ if } X(t) > \alpha, \\ -1, \text{ if } X(t) < \beta, \\ 1, \text{ if } X(t) \in (\beta, \alpha) \text{ and } X(t_-) = \alpha, \\ -1, \text{ if } X(t) \in (\beta, \alpha) \text{ and } X(t_-) = \beta, \end{cases} \tag{5.1}$$

with t_- is the value of time at which the last threshold (α or β) was attained.

The noise might have different characteristics when the system is in one state compared to the other (the transition may involve changes leading to different

M. Dimian and P. Andrei, *Noise-Driven Phenomena in Hysteretic Systems*,
Signals and Communication Technology 218, DOI: 10.1007/978-1-4614-1374-5_5,

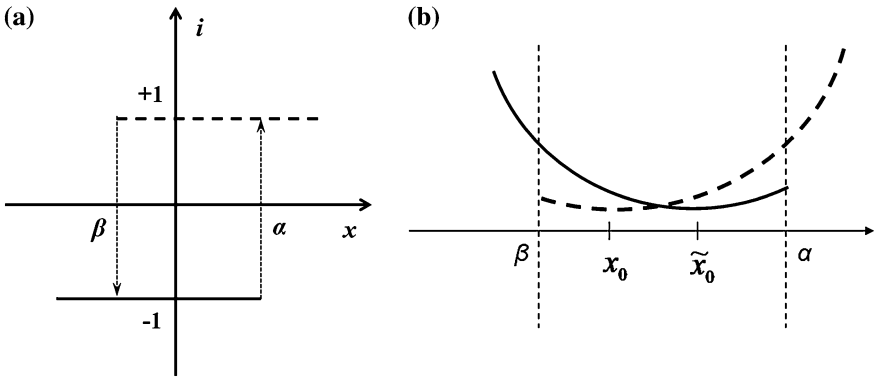

Fig. 5.1 **a** The input–output (x, i) diagram of a bistable system characterized by a rectangular loop; **b** Potential wells for the Brownian motion representing the noise characterization for the two metastable states in the case of OU input

internal noise characteristics). Thus, the input process $X(t)$ is assumed to be described by the Itô stochastic differential equations:

$$dX(t) = b_{\pm 1}(X(t))dt + \sigma_{\pm 1}(X(t))dW(t) \tag{5.2}$$

where $W(t)$ is the Wiener process, while $b_{\pm}$ and $\sigma_{\pm}$ are the drift and diffusion coefficients characterizing the process in +1 and −1, respectively.

In the particular case of Ornstein-Uhlenbeck (OU) processes, we considered $b_{+1}(x) = -b(x - x_0)$, $b_{-1}(x) = -b(x - \tilde{x}_0)$, and $\sigma_{\pm 1}(x) = \sigma$. Since the OU process can be interpreted as a Brownian motion in a parabolic potential, the noise in state +1 can be related to the potential represented by interrupted lines in Fig. 5.1b while the noise in state −1 can be related to the potential represented by the continuous line in Fig. 5.1b.

The autocorrelation function of the output process is:

$$C_I(\tau) = E\{I(\tau) \cdot I(0)\} = \sum_{i_\tau = \pm 1} \sum_{i_0 = \pm 1} i_\tau \cdot i_0 \cdot \rho(i_\tau, i_0) \tag{5.3}$$

where $E\{...\}$ denotes the expected value, while $\rho(i_\tau, i_0)$ is the joint probability density function. The latter is usually found from the product of the transition probability function $\rho(i_\tau | i_0)$ and the stationary probability distribution $\rho_s(i_0)$ for the given process:

$$\rho(i_\tau, i_0) = \rho(i_\tau | i_0)\rho_s(i_0) \tag{5.4}$$

According to Wiener-Khinchine theorem [1], the output spectral density can be expressed as the Fourier transform of the autocorrelation function:

$$S_i(\omega) = 2\mathrm{Re}\left\{\int_0^\infty C_i(\tau)e^{-j\omega\tau}d\tau\right\} \tag{5.5}$$

Although the computation of the spectral density might seem straightforward from the above presentation of the problem there is a fundamental difficulty in finding the autocorrelation function in Eq. (5.3): the hysteretic systems, even in their simplest forms, are memory dependent, and consequently, the output processes are non-Markovian. As a result, the classical approach for the calculation of autocorrelation function involves the Chapman-Kolmogorov equation for the transition probability function, which is not available for non-Markovian processes. Here, the mathematical theory of diffusion processes defined on graphs [2–4] introduced in Sect. 2.2 is used to overcome these difficulties. The presentation follows the line of articles [5–8] published by our group.

5.1.2 *Embedding Output Process into a Markovian Process Defined on Graph*

One can notice for a bistable hysteretic system that the joint specification of current values of input and output leads to a two dimensional stochastic process that has no memory dependence. As a result, the non-Markovian output process $I(t)$ of this system can be embedded into a two-component stochastic process $\mathbf{Z}(t) = (I(t), X(t))$ that is a Markovian process defined on graph Z shown in Fig. 5.2. According to the theory of stochastic processes on a graph, the transition probability function $\rho(\mathbf{z}_t|\mathbf{z}_0)$ for the process $\mathbf{Z}(t)$ satisfies the following forward Kolmogorov equation:

$$\frac{\partial\rho(\mathbf{z}_t|\mathbf{z}_0)}{\partial t} + \hat{L}_x^n\rho(\mathbf{z}_t|\mathbf{z}_0) = 0 \tag{5.6}$$

where $\hat{L}_x^n$ is the second order differential operator associated to the input noise process for each edge $\mathrm{E_n}$ of the graph. For the diffusion process (5.2) this operator has the following expression:

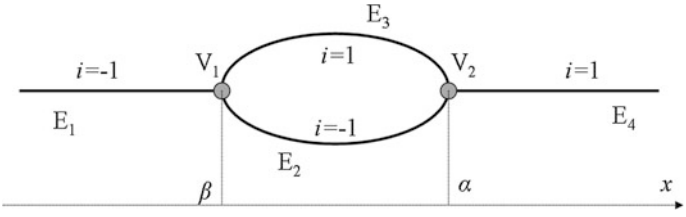

Fig. 5.2 The graph Z on which the diffusion process $\mathbf{Z}(t)$ is defined

$$\left(\hat{L}_x^n f\right)(x) = -\frac{1}{2}\frac{\partial^2}{\partial x^2}\left[\sigma_n^2(x) f(x)\right] + \frac{\partial}{\partial x}\left[b_n(x) f(x)\right] \tag{5.7}$$

The initial condition for the transition probability function has a δ distribution concentrated at $\mathbf{z}_0$. In addition, the solution should decay to zero when x approaches infinity and should satisfy certain boundary conditions at the graph vertices V_1 ($x = \beta$) and V_2 ($x = \alpha$). These vertex boundary conditions characterize the behavior of process $\mathbf{Z}(t)$ at the interior vertices, relating the transition probability functions that corresponds to different edges connected to a specific vertex. According to the theory of Markovian processes on graphs presented in Refs. [2–9] and summarized in Sect. 2.2 of this book, these gluing relations ensure a well-defined Markovian process on the entire graph and depend on the time spent in the vertex under consideration by the process and the probabilities that the process will "move" from the vertex along the edges connected to it.

Since our process has no delay on the vertices and there is zero probability to move from vertex V_1 along edge E_3, while random motion along the edges E_1 and E_2 are equally probable, we arrive at the following vertex boundary conditions for the process $\mathbf{Z}(t)$ at vertex V_1 ($x = \beta$):

$$\rho(\mathbf{z}_t = (-1,\ \beta^-)|\mathbf{z}_0) = \rho(\mathbf{z}_t = (-1,\ \beta^+)|\mathbf{z}_0),\ \rho(\mathbf{z}_t = (1,\ \beta^+)|\mathbf{z}_0) = 0,$$

$$\frac{\partial \rho}{\partial x}(\mathbf{z}_t = (-1,\ \beta^-)|\mathbf{z}_0) = \frac{\partial \rho}{\partial x}(\mathbf{z}_t = (-1,\ \beta^+)|\mathbf{z}_0) + \frac{\partial \rho}{\partial x}(\mathbf{z}_t = (1,\ \beta^+)|\mathbf{z}_0) \tag{5.8}$$

Here β^+ and β^- account for the right and left limits of the function, respectively.

In other words, these vertex boundary conditions express the continuity of the transition probability function when the move from one edge to another happens without switching the output value i and zero boundary condition is imposed on the third edge connected to that vertex. In addition, the probability current must be conserved at each vertex. Analogous boundary conditions are derived for vertex V_2 ($x = \alpha$). In the particular case of the OU process, similar initial-boundary-value problems for the transition probability function have been postulated in [10, 11]. Here, the initial-boundary-value problem is defined on a graph and it was derived based on the theory of diffusion processes on graphs introduced in Sect. 2.2.

In conclusion, the transition probability function for Markovian process $\mathbf{Z}(t)$ is completely defined as the solution of the initial boundary value stated above. Consequently, it can be used to compute the correlation matrix for Markovian process $\mathbf{Z}(t)$:

$$\mathbf{C}_{\mathbf{Z}}(\tau) = \int_{-\infty}^{\infty}\int_{-\infty}^{\infty}\sum_{i_\tau, i_0}\mathbf{z}_\tau^T \mathbf{z}_0 \rho(\mathbf{z}_\tau|\mathbf{z}_0)\rho_s(\mathbf{z}_0)dx_\tau dx_0 \tag{5.9}$$

where $\mathbf{z}^T$ denotes the transpose of vector $\mathbf{z}$, while ρ_s is the stationary distribution of process $\mathbf{Z}(t)$ satisfying the time-independent boundary value problem

corresponding to the initial-boundary value problem stated above. Explicitly, it is the solution of the following set of equations:

$$\frac{1}{2}\frac{\partial^2}{\partial x^2}\left[\sigma_n^2(x)\rho_s(i,x)\right] - \frac{\partial}{\partial x}\left[b_n(x)\rho_s(i,x)\right] = 0 \tag{5.10}$$

defined on each edge E_n of the graph Z which satisfies the time independent vertex boundary conditions at vertex V_1:

$$\rho_s\left(-1,\beta^+\right) = \rho_s(-1,\beta^-),\ \rho_s\left(1,\beta^+\right) = 0, \tag{5.11}$$

similar V_2 conditions, and it decays to 0 at infinity.

Auto-correlation function $C_I(\tau)$ of the output process for a bistable system with hysteresis can be now seen and computed as the first element of the correlation matrix (5.9) for Markovian process $\mathbf{Z}(t)$. Therefore, the fundamental difficulty related to the non-Markovian property of output process $I(t)$ was circumvented by embedding the process into two-component Markovian process $\mathbf{Z}(t)$ defined on graph Z. We have now a well-defined path to compute the autocorrelation function of the output process and its spectral density. Since the complexity of these calculations is relatively high, several techniques are next used to reduce this complexity and to derive a closed form expression for the spectral density.

5.1.3 Closed Form Expression for Output Spectral Density

The spectral density for output process $I(t)$ is the first element of the spectral density matrix of process $\mathbf{Z}(t)$, which is the Fourier transform of the correlation matrix given in (5.9). Once the solutions for the transition probability functions and stationary distribution are found from initial boundary value problem (5.6–5.8) and boundary value problem (5.10, 5.11), respectively, the correlation matrix (5.9) can be computed and, by taking its Fourier transform, one can compute the spectral density. However, this computation can be significantly simplified by the introduction of an auxiliary function:

$$g(\mathbf{z},\ t) = \int_{-\infty}^{\infty} \sum_{i_0} i_0\, \rho(\mathbf{z}_t = \mathbf{z}|\mathbf{z}_0)\rho_s(\mathbf{z}_0)\, dx_0 \tag{5.12}$$

and its half-line Fourier transform:

$$G(\mathbf{z},\omega) = \int_0^{\infty} g(\mathbf{z},\tau)e^{-j\omega\tau}d\tau \tag{5.13}$$

By using the previous definitions and relations, it can be proven that the latter function is the solution of the following equation:

$$j\omega\, G(\mathbf{z},\omega) + L_x^n G(\mathbf{z},\omega) = i\rho_s(\mathbf{z}) \tag{5.14}$$

subject to certain vertex boundary conditions. The spectral density for the output process $I(t)$ can be directly expressed in terms of $G(\mathbf{z},\omega)$:

$$S(\omega) = 2\mathrm{Re}\left\{ \int_{-\infty}^{\infty} \sum_{i=\pm 1} i\, G(\mathbf{z},\omega)\, dx \right\} \tag{5.15}$$

Moreover, since $(i/j\omega)\rho_s(\mathbf{z})$ is a particular solution of inhomogeneous Eq. (5.14), the function defined as:

$$G^0(\mathbf{z},\omega) = G(\mathbf{z},\omega) - \frac{i}{j\omega}\rho_s(\mathbf{z}) \tag{5.16}$$

is the solution of the homogeneous equation:

$$j\omega\, G^0(\mathbf{z},\omega) + L_x^n G^0(\mathbf{z},\omega) = 0 \tag{5.17}$$

subject to certain vertex boundary conditions. The particular solution of Eq. (5.14) stated above has only an imaginary part, and consequently, it does not contribute to the spectral density, which can be then written in the following form:

$$S(\omega) = 2\mathrm{Re}\left\{ \int_{-\infty}^{\infty} \sum_{i=\pm 1} i\, G^0(\mathbf{z},\omega)\, dx \right\} \tag{5.18}$$

$G^0(\mathbf{z},t)$ can be expressed in terms of its spatial derivatives by using Eqs. (5.18) and (5.7), fact that leads to the compensation the integral in Eq. (5.18) by the spatial derivative. As a result, the computation of the spectral density is now reduced to finding the solutions of two boundary value problems, one for stationary probability density ρ_s and one for function G^0, and calculating several derivatives of these solutions at vertex points.

For example, in the case of the OU process, the output spectral density can be written as follows:

$$\begin{aligned} S_{\alpha\beta}(\omega) = \frac{2\sigma^2}{\omega}\Bigg\{ &\left[\frac{d\rho_s}{dx}(1,\beta^+) + \frac{d\rho_s}{dx}(-1,\alpha^-)\right] \\ &- \mathrm{Im}\left[\frac{dG^0}{dx}(1,\beta^+,\omega) + \frac{dG^0}{dx}(1,\alpha^+,\omega) - \frac{dG^0}{dx}(1,\alpha^-,\omega)\right]\Bigg\}. \end{aligned} \tag{5.19}$$

The corresponding boundary value problems can be explicitly integrated leading to analytical solutions in terms of the Gaussian functions and integrals, and the parabolic cylinder functions [12].

As a test for this method, let us consider a hard limiter (HL) system, which corresponds to the limit case when $\alpha = \beta = 0$ and, consequently it is described by the following step function:

$$I_{00}(t) = \hat{\gamma}_{00} X(t) = \begin{cases} 1, & \text{if } X(t) \geq 0 \\ -1, & \text{if } X(t) < 0 \end{cases} \tag{5.20}$$

and an Ornstein-Uhlenbeck input process defined by the following SDE:

$$dX(t) = -bX(t)dt + \sigma X(t)dW(t) \tag{5.21}$$

According to the definition of autocorrelation function for the output process:

$$C_{HL}(\tau) = E\{I_{00}(t+\tau) \cdot I_{00}(t)\} = P\{X(t+\tau)X(t) > 0\} - P\{X(t+\tau)X(t) < 0\} \tag{5.22}$$

where the probability of a negative product can be expressed as:

$$P\{X(t+\tau)X(t) < 0\} = \int_0^{\infty} \int_{-\infty}^{0} \rho(x_{t+\tau}, x_t) dx_{t+\tau} dx_t + \int_{-\infty}^{0} \int_0^{\infty} \rho(x_{t+\tau}, x_t) dx_{t+\tau} dx_t \tag{5.23}$$

while the probability of the positive product is simply $1 - P\{X(t+\tau)X(t) < 0\}$.

As it was proved in 2.1.5, the stationary correlation function for the OU process has expression (2.34), so the stationary joint distribution is:

$$\rho(x_{t+\tau}, x_t) = \frac{b}{2\pi\sigma^2\sqrt{1 - e^{-2b\tau}}} \exp\left(-\frac{b}{2\sigma^2(1 - e^{-2bt})} (x_{t+\tau}^2 + x_t^2 - 2e^{-bt} x_{t+\tau} x_\tau) \right) \tag{5.24}$$

By plugging $\rho(x_{t+\tau}, x_t)$ into formula (5.23) and by using the properties of Gaussian integrals, one arrives at following formula for the probability of having a negative product:

$$P\{X(t+\tau)X(t) < 0\} = \frac{1}{2} - \frac{1}{\pi} \arcsin(e^{-b\tau}) \tag{5.25}$$

and a complementary formula for the probability of a positive product:

$$P\{X(t+\tau)X(t) > 0\} = 1 - P\{X(t+\tau)X(t) < 0\} = \frac{1}{2} + \frac{1}{\pi} \arcsin(e^{-b\tau}) \tag{5.26}$$

By plugging the last two expressions into formula (5.22), the autocorrelation of the hard-limiter system is found to be:

$$C_{HL}(\tau) = \frac{2}{\pi} \arcsin(e^{-bt}) \tag{5.27}$$

This result can be traced back to the work of van Vleck [13, 14] and it is often known as "arcsine law". In conclusion, the output spectral density for the hard-limiter system (5.20) driven by the Ornstein-Uhlenbeck process (5.21) has the following analytical expression:

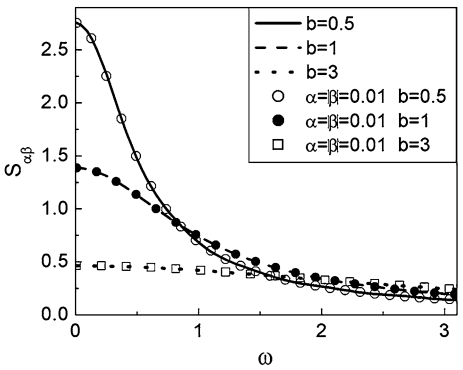

Fig. 5.3 Output spectral densities of the rectangular loop ($\alpha = -\beta = 0.01$; plotted with *symbols*) and the hard limiter system ($\alpha = \beta = 0$; plotted with *lines*) driven by symmetric Ornstein-Uhlenbeck type inputs ($x_0 = \tilde{x}_0$) for selected values of the drift coefficient $b = 0.5$, 1, and 3. (© 2008 NANO, [7])

$$S_{HL}(\omega) = \frac{4}{\pi}\int_0^\infty \arcsin\left(e^{-bt}\right)\cos(\omega t)dt \tag{5.28}$$

It is expected the output spectral density for a rectangular loop should approach the output spectral density of a HL system when thresholds α and β tend to zero. Consequently, formula (5.19) can be tested in this limit case against the classical formula (5.28). The results of this comparison featured an excellent agreement between the two approaches, as it is also apparent from Fig. 5.3. Let us notice that the diffusion coefficient of the input process does not influence the spectral density for the hard-limiter system.

5.1.4 Spectral Analysis of a Bistable Hysteretic System

Next, we examine the influence of the input parameters and system characteristics on the spectral density $S_{\alpha\beta}(\omega)$ of the output of a rectangular loop based on Refs. [6–9]. Besides the interest in its own right, this analysis will be also useful for the understanding of the spectral density of Preisach systems. In Fig. 5.4, the dependence of the spectral noise density on the loop width is presented. For narrow loops, the spectral noise density is similar to the one of a step operator (hard limiter system) where the region of the white noise is connected to the region of $1/f^2$ noise through an intermediate region of $1/f$ behavior (the frequency $f = \omega/2\pi$). This intermediate frequency region is reduced as the loop is broadened, and the variations of the loop width lead mostly to self-similar transformations of the spectral noise density graph. Another interesting observation that emerges from this analysis is related to the transformation of the spectral band. It is known that memoryless nonlinearities broaden spectral bands. However, memory effects may lead to opposite results as shown in Fig. 5.4.

By analyzing the formula for $S_{\alpha\alpha}(\omega)$ and the related boundary-value problems, the following scaling property can be derived:

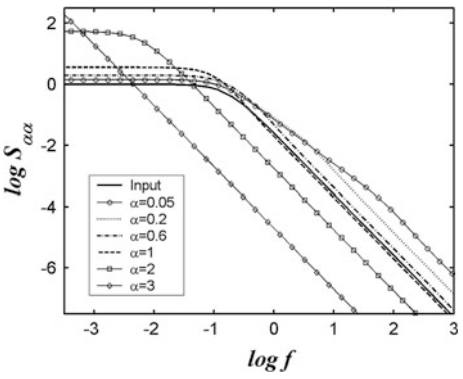

Fig. 5.4 Spectral density $S_{\alpha\alpha}$ of a rectangular loop for various widths of the loop α plotted in a *log–log* scale. The Ornstein-Uhlenbeck input parameters are: $b = \sigma$=1, $x_0 = \tilde{x}_0 = 0$. (© 2004 APS, [6])

$$S_{\alpha\alpha}((x_0, b, \sigma), \omega) = \left(\frac{\alpha}{\sigma}\right)^2 S_{11}\left(\left(\frac{x_0}{\alpha}, b\left(\frac{\alpha}{\sigma}\right)^2, 1\right), \omega\left(\frac{\alpha}{\sigma}\right)^2\right) \tag{5.29}$$

The advantage provided by formula (5.29) is that the computation of the output spectral density for a symmetric rectangular loop with OU inputs is reduced to the computation of the spectral density S_{11}.

The effect of the input stationary average x_0 can be seen from Fig. 5.5. It is apparent that when x_0 is increased, output signals "stabilize" around +1 and, consequently, the spectral noise density is diminished. The influence of the drift coefficient b (or its inverse that represents the correlation time of the input process) on the output spectral density is represented in Fig. 5.6. Thus, sample noise spectra for a hard limiter system ($\alpha = \beta = 0$) are plotted in Fig. 5.6a, while sample spectra for a rectangular loop with $\alpha = -\beta = 1$ are plotted in Fig. 5.6b. In the insets of the two figures, the level of flat spectrum region is plotted against b. As it is apparent from the two figures and their insets, the influence of input noise temporal correlation on the output spectra is quite different when the loop width is negligible with respect to noise strength than in the case when the two are comparable. When the noise strength is dominant ($\alpha - \beta \ll \sigma$), the system behaves as a hard limiter system: The bandwidth of the output spectrum is narrowing, and the

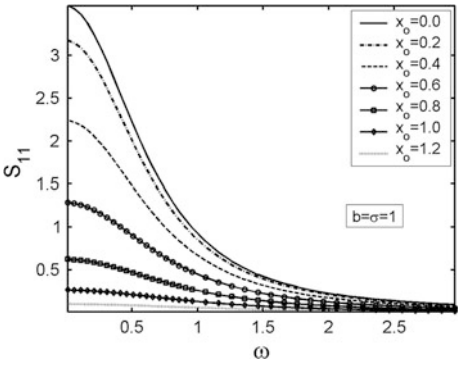

Fig. 5.5 Spectral density S_{11} for various values of the input average value x_0 ($b = \sigma = 1$). (© 2004 APS, [6])

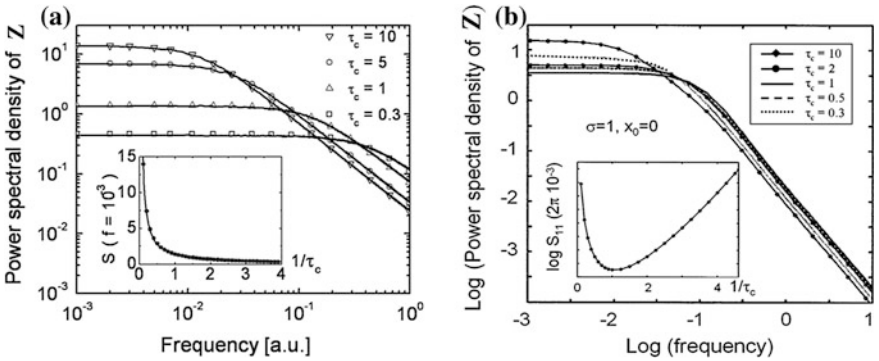

Fig. 5.6 (**a**) Power spectral density for a hard limiter system for selected values of correlation time $\tau_c = 1/b$ plotted in a *log–log* scale ($\sigma = 1$, $x_0 = 0$); in the inset, the level of flat spectrum region is plotted against b; (**b**) Spectral density S_{11} for selected values of the correlation time $\tau_c = 1/b$ plotted in a *log–log* scale ($\sigma = 1$, $x_0 = 0$); in the inset, the level of flat spectrum region against b. (© 2010 IEEE, [8])

level of flat spectrum region is increasing as the correlation time increases (see the inset of Fig. 5.6a). When the memory property becomes prominent, the monotonic behavior presented above is no longer valid, and some extrema for the flat spectrum level and bandwidth appear at some specific correlation time (see the inset of Fig. 5.6b).

These analytical results are also providing the opportunity to test the Monte-Carlo approach to modeling and simulation noise induced phenomena in hysteretic systems presented/and tested for thermal relaxation phenomena in the previous chapter. A very good agreement is observed between the numerical simulations and the analytical results for the spectral analysis of rectangular loops driven by Ornstein-Uhlenbeck noise, which demonstrates the reliability and accuracy of Monte-Carlo technique developed for stochastic hysteretic system.

By these numerical means implemented in HysterSoft©, the spectral analysis of rectangular loop driven by colored noise can be performed. When the noise spectrum increases with frequency as f^2, so-called *violet* noise, the output spectrum stays almost constant for most of the frequency interval, except for high-frequency region where it features an increase slightly higher than a linear dependence of f. When the noise spectrum increases with frequency as f, so-called *blue* noise, a similar behavior is observed for low-frequency region, while a slight spectrum increase is observed for high-frequency region. The simulations performed for various input power-law spectrum f^λ, $\lambda > 0$, lead to the conclusion that the corresponding output spectra feature a flat region for low-frequency region and a power law with an exponent slightly different than for high frequency.

The behavior corresponding to a power-law input spectrum f^λ, $\lambda < 0$, is significantly different than the one described above. When the noise spectrum is proportional to $1/f$, coined as *pink* noise, the output spectrum follows a similar pattern for low frequency, with an exponent slightly higher than 1, while a $1/f^2$

behavior is present for high frequencies. When the noise spectrum is proportional to $1/f^2$, known as *Brownian* noise, the output spectrum follows a similar behavior, except that the exponent is slightly higher than 2 for low-frequency region. The decay in the output spectra for high frequency was common to all power-law input spectra with considered in our analysis.

Sample of these simulations for output spectrum of rectangular loop $\hat{\gamma}_{-1,1}$ driven by colored Gaussian noise are shown in Fig. 5.7. By using HysterSoft© the reader can generate a wide variety of colored noises and analyze their spectral transformation by a general bistable system with hysteretic rectangular loop.

Next, let us consider that noise has different characteristics in one state of the system than in the other. As a case study, we take a noise described by an OU

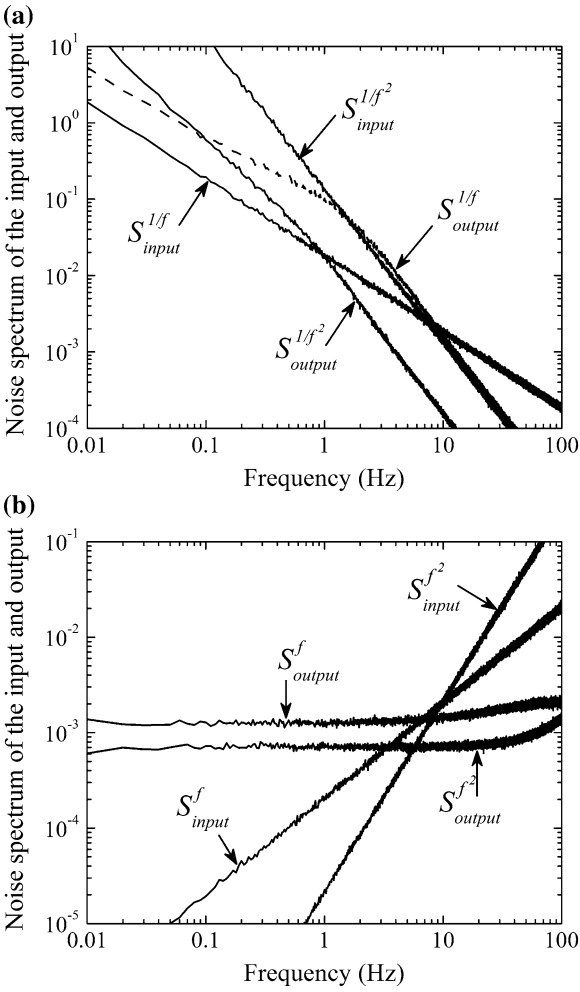

Fig. 5.7 Noise input spectrum and the corresponding output spectrum for rectangular loop $\hat{\gamma}_{-1,1}$ in the case of (**a**) *pink* Gaussian noise input ($1/f$) and *Brownian* noise input ($1/f^2$); (**b**) *blue* Gaussian noise input (f) and *violet* Gaussian noise input (f^2)

process with $b_{+1}(x) = -b(x - x_0)$ in +1 state and by an OU process with $b_{-1}(x) = -b(x - \tilde{x}_0)$ in -1 state, while diffusion coefficient is the same in both states. As mentioned above, noise in state +1 can be interpreted as a Brownian motion in a parabolic potential represented by the interrupted line in Fig. 5.1b while the noise in state -1 can be interpreted as a Brownian motion in a parabolic potential represented by the continuous line in Fig. 5.1b. In the case of symmetric noise ($x_0 = \tilde{x}_0$), the monotonic behavior of the output spectral density with respect to the frequency is a common feature of bistable hysteretic system. The symmetry breaking ($x_0 \neq \tilde{x}_0$) can lead to non-monotonic behavior and more precisely to the appearance of a maximum in the output spectra, as can be observed from Fig. 5.8 obtained by using Eq. (5.19). That can be related to the manifestation of an almost regular behavior of the system output, so pure noise input can lead to almost periodic sequences of -1 and 1. This noise induced phenomena is known as *coherence resonance* [11, 15].

In conclusion, output power spectral density of bistable hysteretic systems with diffusion input has been found by analytical means by using the theory of stochastic processes on graphs. In the particular case of OU input, the output spectra have been explicitly computed and analyzed, discussing the influence of input drift and diffusion coefficients, as well as of the rectangular loop width on the output spectra characteristics. While it is mostly experienced as a disruptive effect, noise can also have a constructive role, activating a resonance response of the system. It was proven that certain bistable hysteretic systems driven by "state-dependent" noise inputs manifest of an almost regular behavior of the system output. The spectrum of bistable hysteretic system driven by colored noise has been analyzed by numerical means using the Monte-Carlo method presented in Chap. 2. Since complex hysteretic nonlinearities with stochastic input can be described through Preisach formalism as weighted superposition of stochastically driven rectangular loop operators, this analysis is also useful for better understanding of spectra in complex hysteretic systems such as the ones discussed in the next sections.

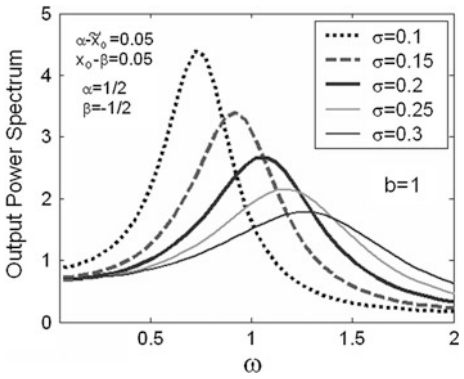

Fig. 5.8 Output spectral densities of the rectangular loop ($\alpha = -\beta = 0.5$) driven by asymmetric Ornstein-Uhlenbeck type inputs for selected values of the diffusion coefficient σ. (© 2008 NANO, [7])

5.2 Spectral Density of Symmetric Preisach Systems with Diffusion Input: Analytical Approach

In this section, closed form expressions for the spectral densities of symmetric Preisach hysteretic systems driven by diffusion inputs are found by analytical means. The theory of stochastic processes on graphs is used to circumvent the difficulties related to the non-Markovian property of the output of hysteretic systems, while the explicit calculations are appreciably simplified by the introduction of the "effective" distribution function. The implementation of the method for the case of Ornstein-Uhlenbeck process is presented in detail and general qualitative features of these spectral densities are examined. Due to the universality of the Preisach model, this approach can be used to describe hysteresis nonlinearities of various physical origins.

5.2.1 Statement of the Problem

Consider complex hysteretic nonlinearities that can be modeled through the Preisach formalism (see Sect. 1.2) as weighted superposition of rectangular loops. For many hysteretic systems (especially magnetic materials), the Preisach distribution is narrowly peaked around the diagonal line $\alpha = -\beta$ and consequently, it can be approximated by $\mu(\alpha)\delta(\alpha + \beta)$. For these materials, the symmetric Preisach model is constructed as a weighted superposition of symmetric rectangular loops $\hat{\gamma}_\alpha = \hat{\gamma}_{\alpha(-\alpha)}$ with the weight function $\mu(\alpha)$ which will be considered Preisach distribution for that symmetric system. Thus the symmetric Preisach model takes the following form:

$$y(t) = \int_0^{\alpha_0} \hat{\gamma}_\alpha x(t)\mu(\alpha)d\alpha = \int_0^{\alpha_0} i_\alpha(t)\mu(\alpha)d\alpha \tag{5.30}$$

where:

$$i_\alpha(t) = \hat{\gamma}_\alpha x(t) = \begin{cases} 1, \text{ if } x(t) > \alpha, \\ -1, \text{ if } x(t) < -\alpha, \\ 1, \text{ if } x(t) \in (-\alpha, \alpha) \text{ and } x(t_-) = \alpha, \\ -1, \text{ if } x(t) \in (-\alpha, \alpha) \text{ and } x(t_-) = -\alpha, \end{cases} \tag{5.31}$$

with t_- is the value of time at which the last threshold (α or $-\alpha$) was attained.

The input process $x(t)$ is assumed to be described by the Itô stochastic differential equation:

$$dX(t) = b(X(t))dt + \sigma(X(t))dW(t) \tag{5.32}$$

where $W(t)$ is the Wiener process, while b and σ are the drift and diffusion coefficients, respectively. The stochastic nature of the input leads to random switchings of the rectangular loop operators $\hat{\gamma}_\alpha$ and, therefore, the output of the Preisach model is a stochastic process as well, denoted by $Y(t)$.

The autocorrelation function of the output process $Y(t)$ is:

$$C_Y(\tau) = E\{Y(\tau)Y(0)\} = \int_0^{\alpha_0}\int_0^{\alpha_0} E\left\{\hat{\gamma}_\beta X(\tau)\hat{\gamma}_\alpha X(0)\right\}\mu(\beta)\mu(\alpha)d\beta d\alpha\,, \tag{5.33}$$

Thus, we can express the autocorrelation function as a weighted superposition of cross-correlation functions $C_{\beta\alpha}(\tau)$ of two-dimensional processes $(I_\beta(t),\ I_\alpha(t))$, representing the outputs of two symmetric rectangular loops:

$$C_Y(\tau) = \int_0^{\alpha_0}\int_0^{\alpha_0} C_{\beta\alpha}(\tau)\mu(\beta)\mu(\alpha)d\beta d\alpha, \tag{5.34}$$

Cross-correlation functions $C_{\beta\alpha}(\tau)$ are not even functions, but $C_{\beta\alpha}(-\tau) = C_{\alpha\beta}(\tau)$ and consequently, the correlation function of the Preisach system $C_Y(\tau)$ is even.

According to the Wiener-Kinchine theorem [10], the process's spectral density is the Fourier Transform of the autocorrelation function. Because we deal with an even correlation function, the spectral density of the output process can be expressed as:

$$S_Y(\omega) = 2\mathrm{Re}\left\{\int_0^\infty C_Y(\tau)e^{-j\omega\tau}d\tau\right\} = \int_0^{\alpha_0}\int_0^{\alpha_0} S_{\beta\alpha}(\omega)\mu(\beta)\mu(\alpha)d\beta d\alpha, \tag{5.35}$$

where $S_{\beta\alpha}(\omega)$ is the "cross-spectral density" for the two-dimensional process $(I_\beta(t),\ I_\alpha(t))$ and it is related to the cross-correlation function $C_{\beta\alpha}(\tau)$ as follows:

$$S_{\beta\alpha}(\omega) = 2\mathrm{Re}\left\{\int_0^\infty C_{\beta\alpha}(\tau)e^{-j\omega\tau}d\tau\right\}. \tag{5.36}$$

5.2.2 Calculation Method for the Output Correlation Function Using Markovian Processes on Graphs

The Preisach model describes hysteresis nonlinearities with non-local memories. For this reason, the output process $Y(t)$ cannot be embedded as a component of some finite-dimensional Markov process. However, the previous expression shows that this spectral density can be expressed as a weighted superposition of spectral

densities for much simpler processes ($I_\beta(t)$, $I_\alpha(t)$). These processes are still non-Markov, but they can be embedded in higher dimensional Markov processes.

In order to compute $S_{\beta\alpha}(\omega)$, let us consider the three component process $\mathbf{Z}(t) = \big(I_\beta(t), I_\alpha(t), X(t)\big)$. Because the rectangular loop operators describe hysteresis with local memory, the joint specification of current values of input and output uniquely define the states of this hysteresis. As a result, $\mathbf{Z}(t)$ is a Markovian process. In addition, only certain combinations of $I_\beta(t)$, $I_\alpha(t)$ and $X(t)$ are possible, and they are presented on the graph Z shown in Fig. 5.9. The binary process $I_\beta(t)$ and $I_\alpha(t)$ assume constant values on edges of the graph Z.

Applying the theory of stochastic processes on graphs (see Sect. 2.2.2), the following initial-boundary value problem for the transition probability density function $\rho(\mathbf{z}, t|\mathbf{z}', 0)$ of the Markovian process $\mathbf{Z}(t)$ defined on the graph Z can be derived. On each edge of this graph, $\rho(\mathbf{z}, t|\mathbf{z}', 0)$ satisfies the following forward Kolmogorov equation:

$$\frac{\partial \rho(\mathbf{z}, t|\mathbf{z}', 0)}{\partial t} + L_x \rho(\mathbf{z}, t|\mathbf{z}', 0) = 0 \tag{5.37}$$

where $\hat{L}_x$ is the second order elliptic operator associated with the input diffusion process defined in (5.32) and is specified by the expression:

$$\hat{L}_x \rho = -\frac{1}{2}\frac{\partial^2}{\partial x^2}\left(\sigma^2(x)\rho\right) + \frac{\partial}{\partial x}\left(b(x)\rho\right) \tag{5.38}$$

The function $\rho(\mathbf{z}, t|\mathbf{z}', 0)$ satisfies the initial conditions:

$$\rho(\mathbf{z}, 0|\mathbf{z}', 0) = \delta_{i_\beta i'_\beta}\delta_{i_\alpha i'_\alpha}\delta(x, x') \tag{5.39}$$

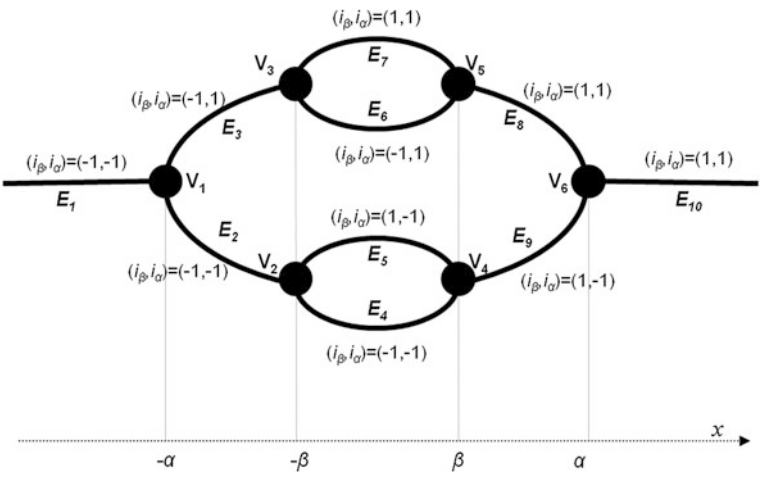

Fig. 5.9 The graph on which three component process Z is defined

and it has to decay to zero for x going to infinity. In addition, the so-called "vertex" type boundary conditions (2.73) at graph vertices have to be satisfied. These "vertex" type boundary conditions express the continuity of the transition probability density when the transition from one graph edge occurs without switching of the rectangular loop, and zero boundary condition is imposed on the third graph edge connected to this vertex. Moreover, the probability current has to be conserved at each vertex. For example, at the vertex V_1 (corresponding to $x = -\alpha$, in the case $\alpha > \beta$), these conditions are explicitly written as:

$$\begin{aligned}
&\rho((-1,-1,-\alpha^+),t|\mathbf{z}',0) = \rho((-1,-1,-\alpha^-),t|\mathbf{z}',0),\\
&\rho((-1,1,-\alpha^+),t|\mathbf{z}',0) = 0,\\
&\frac{\partial\rho}{\partial x}((-1,1,-\alpha^+),t|\mathbf{z}',0) + \frac{\partial\rho}{\partial x}((-1,-1,-\alpha^+),t|\mathbf{z}',0) = \frac{\partial\rho}{\partial x}((-1,-1,-\alpha^-),t|\mathbf{z}',0).
\end{aligned} \tag{5.40}$$

It is apparent that the stationary probability density of the process $\mathbf{Z}(t)$ is the solution of the following boundary value problem:

$$\begin{cases} \hat{L}_x\rho_s(\mathbf{z}) = 0 \text{ on each graph edge,} \\ \text{"vertex" boundary conditions at each graph vertex.} \end{cases} \tag{5.41}$$

Taking into account the facts presented above, the cross-correlation function $C_{\beta\alpha}(\tau)$ can be seen as a component of the correlation matrix $\boldsymbol{C}_{\mathbf{Z}}(\tau)$ for the Markov process $\mathbf{Z}(t)$:

$$\begin{aligned}
\mathbf{C}_{\mathbf{Z}}(\tau) = E\{\mathbf{Z}^T(\tau)\mathbf{Z}(0)\} &= \int_{-\infty}^{\infty}\int_{-\infty}^{\infty}\sum_{i_\alpha,i_\beta}\sum_{i'_\alpha,i'_\beta}\mathbf{z}^T\mathbf{z}'\rho(\mathbf{z},\tau;\mathbf{z}',0)dxdx'\\
&= \int_{-\infty}^{\infty}\int_{-\infty}^{\infty}\sum_{i_\alpha,i_\beta}\sum_{i'_\alpha,i'_\beta}\mathbf{z}^T\mathbf{z}'\rho(\mathbf{z},\tau|\mathbf{z}',0)\rho_s(\mathbf{z}')dxdx'
\end{aligned} \tag{5.42}$$

In the above formula, the sums are taken over all graph values of the (i_β, i_α) and (i'_β,i'_α), respectively. This convention is maintained throughout the book.

5.2.3 Closed Form Expression for the Output Spectral Density

To simplify the computation of the cross-correlation function, the "effective" distribution function $g(\mathbf{z},\tau)$ is introduced:

$$g(\mathbf{z},\tau) = \int_{-\infty}^{\infty}\sum_{i'_\alpha,i'_\beta} i'_\alpha\rho(\mathbf{z},\tau|\mathbf{z}',0)\rho_s(\mathbf{z}')dx' \tag{5.43}$$

A similar function has been previously proposed in [16] and used in the analysis of noise in semiconductor devices.

By using Eq. (5.37) on each edge of the graph, the initial condition (5.39), and "vertex" type boundary conditions for transition probability density, as well as boundary value problem (5.41) for stationary probability density, one can derive the following initial boundary value problem for the "effective" distribution function:

$$\begin{cases} \frac{\partial g(\mathbf{z},\tau)}{\partial \tau} + L_x g(\mathbf{z},\tau) = 0 \text{ on each graph edge}, \\ g(\mathbf{z},0) = i_\alpha \rho_s(\mathbf{z}), \\ \lim\limits_{x\to\pm\infty} g(\mathbf{z},\tau) = 0, \\ \text{``vertex'' boundary conditions}. \end{cases} \tag{5.44}$$

Using formulas (5.42) and (5.43) the cross-correlation function $C_{\beta\alpha}(\tau)$ can be expressed by the formula:

$$C_{\beta\alpha}(\tau) = \int\limits_{-\infty}^{\infty} \sum_{i_\alpha, i_\beta} i_\beta g\big((i_\beta, i_\alpha, x), \tau\big) dx \tag{5.45}$$

Thus, in order to find the cross-correlation function $C_{\beta\alpha}(\tau)$, one has to solve first the boundary value problem (5.41) for stationary distribution $\rho_s(\mathbf{z})$, then the initial-boundary value problem (5.44) for the "effective" distribution function $g(\mathbf{z},\tau)$, and finally to compute integral (5.45). According to the Eq. (5.36), another integration has to be performed for the computation of the cross-spectral density $S_{\beta\alpha}(\omega)$. However, by introducing the one-side Fourier transform of the "effective" distribution function:

$$G(\mathbf{z},\omega) = \int\limits_{0}^{\infty} g(\mathbf{z},\tau) e^{-j\omega\tau} d\tau \tag{5.46}$$

the cross-spectral density $S_{\beta\alpha}(\omega)$ can be written in the form:

$$S_{\beta\alpha}(\omega) = 2\mathrm{Re}\left\{ \int\limits_{0}^{\infty} \sum_{i_\alpha, i_\beta} i_\beta G(\mathbf{z},\omega) dx \right\} \tag{5.47}$$

Performing the Fourier transformation of the initial-boundary-value problem (5.44), we arrive at the following boundary-value problem for $G(\mathbf{z},\omega)$:

$$\begin{cases} j\omega G(\mathbf{z},\omega) + L_x G(\mathbf{z},\omega) = i_\alpha \rho_s(\mathbf{z}) \text{ on each graph edge}, \\ \lim\limits_{x\to\pm\infty} G(\mathbf{z},\omega) = 0, \\ \text{"vertex" boundary conditions}. \end{cases} \tag{5.48}$$

For example, these "vertex" boundary conditions at vertex V_1 ($x = -\alpha$) are:

$$\begin{aligned}
&G((-1,-1,-\alpha^+),\omega) = G((-1,-1,-\alpha^-),\omega),\\
&G((-1,1,-\alpha^+),\omega) = 0,\\
&\frac{\partial G}{\partial x}((-1,1,-\alpha^+),\omega) + \frac{\partial G}{\partial x}((-1,-1,-\alpha^+),\omega) = \frac{\partial G}{\partial x}((-1,-1,-\alpha^-),\omega)
\end{aligned} \tag{5.49}$$

Because the stationary probability distribution satisfies the differential equation of the boundary-value problem (5.41), function $(i_\alpha/j\omega)\rho_s(\mathbf{z})$ is (for each ω) a particular solution for the non-homogeneous differential equation in (5.48). Taking into account the linearity of operator L_x, $G(\mathbf{z},\omega)$ can be written as:

$$G(\mathbf{z},\omega) = G^0(\mathbf{z},\omega) + \frac{i_\alpha}{j\omega}\rho_s(\mathbf{z}) \tag{5.50}$$

where $G^0(\mathbf{z},\omega)$ is a solution of the corresponding homogeneous equation. Since the particular solution is purely imaginary, it does not contribute to the cross-spectral density $S_{\beta\alpha}(\omega)$. Thus,

$$S_{\beta\alpha}(\omega) = 2\mathrm{Re}\left\{\int_0^\infty \sum_{i_\alpha, i_\beta} i_\beta G^0(\mathbf{z},\omega)dx\right\} \tag{5.51}$$

with $G^0(\mathbf{z},\omega)$ satisfying the following boundary-value problem:

$$\begin{cases}
j\omega G^0(\mathbf{z},\omega) + L_x G^0(\mathbf{z},\omega) = 0 \text{ on each graph edge,}\\
\lim\limits_{x\to\pm\infty} G^0(\mathbf{z},\omega) = 0,\\
\text{inhomogeneous ``vertex'' - type boundary conditions.}
\end{cases} \tag{5.52}$$

Next, we describe these inhomogeneous "vertex"-type boundary conditions. First, by inspecting "vertex" boundary conditions for $G(\mathbf{z},\omega)$ and $\rho_s(\mathbf{z})$, it can be observed that, when transition from one edge to another occurs without switching of the rectangular loops, $G(\mathbf{z},\omega)$ and $\rho_s(\mathbf{z})$ corresponding to these edges are continuously matched and i_α does not change its value. Consequently, the corresponding $G^0(\mathbf{z},\omega)$ is also continuously matched in this case. On the third edge connected to the vertex, zero boundary condition is valid. Until this point, inhomogeneous "vertex" boundary type conditions coincide with the previous ones. This coincidence is also maintained in the boundary conditions for derivatives at vertices V_{2-5} ($x = \pm\beta$). However, the difference appears in the conditions for derivatives at vertices V_1 and V_6 ($x = \pm\alpha$). Namely, from the boundary condition (5.49) for the derivative of $G(\mathbf{z},\omega)$, we have:

$$\frac{\partial G^0}{\partial x}((-1,1,-\alpha^+),\omega)+\frac{1}{j\omega}\frac{\partial \rho_s}{\partial x}(-1,1,-\alpha^+)+\frac{\partial G^0}{\partial x}((-1,-1,-\alpha^+),\omega)$$
$$+\frac{(-1)}{j\omega}\frac{\partial \rho_s}{\partial x}(-1,-1,-\alpha^+)=\frac{\partial G^0}{\partial x}((-1,-1,-\alpha^-),\omega)+\frac{(-1)}{j\omega}\frac{\partial \rho_s}{\partial x}(-1,-1,-\alpha^-)\,. \tag{5.53}$$

Taking into account the boundary condition for stationary probability distribution, the following boundary condition for $G^0(\mathbf{z},\omega)$ is derived:

$$\frac{\partial G^0}{\partial x}((-1,1,-\alpha^+),\omega)+\frac{\partial G^0}{\partial x}((-1,-1,-\alpha^+),\omega)$$
$$+\frac{2}{j\omega}\frac{\partial \rho_s}{\partial x}(-1,1,-\alpha^+)=\frac{\partial G^0}{\partial x}((-1,-1,-\alpha^-),\omega)\,. \tag{5.54}$$

By using similar arguments, the inhomogeneous "vertex" boundary condition at the vertex V_6 is found to be:

$$\frac{\partial G^0}{\partial x}((1,1,\alpha^-),\omega)+\frac{\partial G^0}{\partial x}((1,-1,\alpha^-),\omega)$$
$$-\frac{2}{j\omega}\frac{\partial \rho_s}{\partial x}(1,-1,-\alpha^+)=\frac{\partial G^0}{\partial x}((1,1,\alpha^+),\omega)\,. \tag{5.55}$$

In the case $\alpha<\beta$, the boundary conditions for vertices corresponding to $x=\mp\alpha$ take the following form:

$$\frac{\partial G^0}{\partial x}\left(\left(i_\beta,1,\mp\alpha^\pm\right),\omega\right)+\frac{\partial G^0}{\partial x}\left(\left(i_\beta,-1,\mp\alpha^\pm\right),\omega\right)$$
$$\pm\frac{2}{j\omega}\frac{\partial \rho_s}{\partial x}\left(i_\beta,\pm1,\mp\alpha^\pm\right)=\frac{\partial G^0}{\partial x}\left(\left(i_\beta,\mp1,\mp\alpha^\mp\right),\omega\right)\,. \tag{5.56}$$

Now, the method for the calculation of the spectral density can be summarized as the sequence of the following steps:

Step 1: Solve boundary value problem (5.41) for stationary distribution $\rho_s(\mathbf{z})$.
Step 2: Solve boundary value problem (5.52) for $G^0(\mathbf{z},\omega)$
Step 3: Calculate cross-spectral density $S_{\beta\alpha}(\omega)$ by using formula (5.51)
Step 4: Calculate spectral density $S_Y(\omega)$ by using formula (5.35).

The following observations can simplify the implementation of the above steps:

1. For a given input, first three steps of the method are independent of Preisach function $\mu(\alpha)$. Therefore, once $S_{\beta\alpha}(\omega)$ are precomputed, they can be used for any "symmetric" Preisach system (5.30). In other words, the spectral density of a hysteretic system can be computed as a weighted superposition of cross-spectral densities $S_{\beta\alpha}(\omega)$ precomputed at the third step, with the weight being given by the Preisach function of that system.

2. As can be observed from Eq. (5.51), the cross-spectral densities $S_{\beta\alpha}(\omega)$ are expressed as linear combinations of $G^0(\mathbf{z}, \omega)$ corresponding to different edges. This indicates that it may not be necessary to find an explicit expression for $G^0(\mathbf{z}, \omega)$ on every edge, but rather their linear combinations mentioned above.
3. By using the expression (5.38) for operator $\hat{L}_x$, an important simplification can be made. From formula (5.52) follows $G^0(\mathbf{z}, \omega) = (j/\omega)\hat{L}_x G^0(\mathbf{z}, \omega)$. By substituting the later expression into formula (5.51), one can obtain:

$$S_{\beta\alpha}(\omega) = 2\mathrm{Re}\left\{\int_0^\infty \sum_{i_\alpha, i_\beta} i_\beta \left(\frac{j}{\omega}\right) \hat{L}_x G^0(\mathbf{z}, \omega) dx\right\}$$
$$= -\frac{2}{\omega}\mathrm{Im}\left\{\int_0^\infty \hat{L}_x \left(\sum_{i_\alpha, i_\beta} i_\beta G^0(\mathbf{z}, \omega)\right) dx\right\}. \tag{5.57}$$

The derivatives in the operator $\hat{L}_x$ can be integrated and this results in a simple expression for the spectral density in terms of the first derivatives of $G^0(\mathbf{z}, \omega)$ at vertex points (see, for example, the next section).

4. The boundary-value problems (5.41) and (5.52) defined on the entire graph Z, can be sequentially reduced to the boundary-value problems defined on the real line intervals which are more tractable analytically and numerically. Efficient numerical algorithms for solving these problems defined on the real line interval are three-diagonal matrix solvers described, for instance, in Ref. [17].

The above observations produce further simplifications in the method for computations of the spectral density once a specific form of the input stochastic process is given. These advantages will be further exploited in the next section where the Ornstein-Uhlenbeck process is used as a model of driving noise.

The proposed method is conceptually valid for Preisach systems with non-symmetric rectangular loops, although the complexity of calculations will be appreciably increased.

5.2.4 *Example: Spectral Density of Symmetric Preisach Systems with Ornstein-Uhlenbeck Input*

In this section we shall apply the method developed in the previous section to the case when the input is an Ornstein-Uhlenbeck (OU) process. As has been discussed in 2.1.5, the OU process satisfies:

$$\hat{L}_x \rho = -b\frac{\partial[(x - x_0)\rho]}{\partial x} - \frac{\sigma^2}{2}\frac{\partial^2 \rho}{\partial x^2} \tag{5.58}$$

Step 1

For the OU input process, the boundary-value problem (5.41) for the stationary distribution of the process $\mathbf{z}(t)$ defined on the graph Z from Fig. 5.9 can be solved by using the first example in Sect. 2.2.3. Thus, by adding the stationary distributions corresponding to edges E_6 and E_7 as well as to edges E_4 and E_5, we end up to the problem solved there and the results are:

$$\begin{aligned}
\tilde{\rho}_1^{st}(x) &= \hat{\rho}^{st}(x), \quad x \in (-\infty, -\alpha) \\
\tilde{\rho}_2^{st}(x) &= \hat{\rho}^{st}(x)(1 - \phi_{-\alpha\alpha}(x)), \quad x \in (-\alpha, \alpha) \\
\tilde{\rho}_3^{st}(x) &= \hat{\rho}^{st}(x)\phi_{-\alpha\alpha}(x), \quad x \in (-\alpha, \alpha) \\
\tilde{\rho}_4^{st}(x) &= \hat{\rho}^{st}(x), \quad x \in (\alpha, \infty)
\end{aligned} \tag{5.59}$$

where

$$\hat{\rho}_s(x) = \sqrt{\frac{b}{\pi\sigma^2}} e^{-b(x-x_0)^2/\sigma^2}, \quad \phi_{a_1a_2}(x) = \frac{\int_{a_1}^{x} e^{b(y-x_0)^2/\sigma^2}}{\int_{a_1}^{a_2} e^{b(y-x_0)^2/\sigma^2}} \tag{5.60}$$

Similarly to the previous derivation, the components of the stationary distributions for edges E_6 and E_7 as well as for edges E_4 and E_5 can be determined leading to the following expression:

$$\rho_s(\mathbf{z}) = \begin{cases}
\hat{\rho}_s(x) \text{ on } E_1 \text{ and} E_{10}, \\
\hat{\rho}_s(x)(1 - \phi_{-\alpha\alpha}(x)) \text{ on } E_2 \text{ and } E_8, \\
\hat{\rho}_s(x)\phi_{-\alpha\alpha}(x) \text{ on } E_3 \text{ and } E_9, \\
\hat{\rho}_s(x)(1 - \phi_{-\alpha\alpha}(x))\big(1 - \phi_{-\beta\beta}(x)\big) \text{ on } E_4, \\
\hat{\rho}_s(x)(1 - \phi_{-\alpha\alpha}(x))\phi_{-\beta\beta}(x) \text{ on } E_5, \\
\hat{\rho}_s(x)\phi_{-\alpha\alpha}(x)\big(1 - \phi_{-\beta\beta}(x)\big) \text{ on } E_6, \\
\hat{\rho}_s(x)\phi_{-\alpha\alpha}(x)\phi_{-\beta\beta}(x) \text{ on } E_7,
\end{cases} \tag{5.61}$$

The results for the case $\alpha < \beta$ are obtained by interchanging α and β.

Step 2

Next, the boundary-value problem (5.52) defined on the graph Z is reduced to boundary-value problems defined on line intervals, which are better tractable both analytically and numerically. This procedure is very useful because it could be applied to Steps 1 and 2 of the method in the case of a general input diffusion process.

First, we formulate the boundary-value problem for $G^0(x, \omega) = \sum_{i_\alpha, i_\beta} G^0(\mathbf{y}, \omega)$, where the sum is taken over all graph edges:

$$\begin{cases}
j\omega G^0(x, \omega) + L_x G^0(x, \omega) = 0, \; x \in (-\infty, +\infty)\backslash\{-\alpha, \alpha\}, \\
\lim\limits_{x \to \pm\infty} G^0(x, \omega) = 0, \\
\frac{\partial G^0}{\partial x}(-\alpha^-, \omega) - \frac{\partial G^0}{\partial x}(-\alpha^+, \omega) = \frac{2}{j\omega}\sqrt{\frac{b}{\pi\sigma^2}}\left(\int_{-\alpha}^{\alpha} e^{b(y-x_0)^2/\sigma^2}\right)^{-1}, \\
\frac{\partial G^0}{\partial x}(\alpha^-, \omega) - \frac{\partial G^0}{\partial x}(\alpha^+, \omega) = -\frac{2}{j\omega}\sqrt{\frac{b}{\pi\sigma^2}}\left(\int_{-\alpha}^{\alpha} e^{b(y-x_0)^2/\sigma^2}\right)^{-1}.
\end{cases} \tag{5.62}$$

The solution of this problem coincides with the solution of problem (5.52) for edges E_1 and E_{10}. In addition, it will also help to simplify the expression for the cross-spectral density.

Second, we formulate the boundary-value problem for $G^0(1,x,\omega) = \sum_{i_\beta} G^0\big((1,i_\beta,x),\omega\big)$, where the sum is taken over "central" graph edges. In the case $\alpha < \beta$, $G^0(1,x,\omega) = \sum_{i_\alpha} G^0((i_\alpha,1,x),\omega)$.

From formulas (5.52) and (5.61), we find:

$$\begin{cases} j\omega G^0(1,x,\omega) + L_x G^0(1,x,\omega) = 0,\ x \in (-\alpha,\alpha), \\ G^0(1,-\alpha,\omega) = 0, \\ G^0(1,\alpha,\omega) = G^0(\alpha,\omega) \end{cases} \tag{5.63}$$

for the case of $\alpha > \beta$ and

$$\begin{cases} j\omega G^0(1,x,\omega) + L_x G^0(1,x,\omega) = 0,\ x \in (-\beta,\beta)\backslash\{-\alpha,\alpha\}, \\ G^0(1,-\beta,\omega) = 0, \\ G^0(1,\beta,\omega) = G^0(\beta,\omega), \\ \\ \frac{\partial G^0}{\partial x}(1,-\alpha^-,\omega) - \frac{\partial G^0}{\partial x}(1,-\alpha^+,\omega) = \frac{2}{j\omega}\sqrt{\frac{b}{\pi\sigma^2}}\frac{\phi_{-\beta\beta}(-\alpha)}{\int_{-\alpha}^{\alpha} e^{b(y-x_0)^2/\sigma^2}}, \\ \\ \frac{\partial G^0}{\partial x}(1,\alpha^-,\omega) - \frac{\partial G^0}{\partial x}(1,\alpha^+,\omega) = -\frac{2}{j\omega}\sqrt{\frac{b}{\pi\sigma^2}}\frac{\phi_{-\beta\beta}(\alpha)}{\int_{-\alpha}^{\alpha} e^{b(y-x_0)^2/\sigma^2}}, \end{cases} \tag{5.64}$$

for the case of $\alpha < \beta$.

It is obvious that $G^0(-1,x,\omega) = G^0(x,\omega) - G^0(1,x,\omega)$ in both cases. The solutions of these problems coincide with the solution of problem (5.52) for edges E_2, E_3 and E_8, E_9. To completely solve problem (5.52), one should find the solution for the "central" edges E_{4-7}. However, it will be shown below that the cross-spectral density can be expressed in terms of the previously found functions, and consequently, the solution of problem (5.52) for these "central" edges is not necessary. Thus, the boundary-value problem (5.52) defined on the entire graph Z was reduced to the boundary-value problems defined on line intervals.

In the case of an OU input process, the specific form of the operator $\hat{L}_x$ is helpful in order to find explicit analytical solution to problem (5.52) in terms of parabolic cylinder functions [12]. Namely, one can observe that if a function $\tilde{f}$ satisfies the differential equation for the parabolic cylinder functions:

$$\frac{\partial^2 \tilde{f}}{\partial \tilde{x}^2}(\tilde{x},\omega) + \left[-\frac{1}{4}\tilde{x}^2 + \left(\frac{1}{2} - j\frac{\omega}{b}\right)\right]\tilde{f}(\tilde{x},\omega) = 0, \tag{5.65}$$

then $f(x,\omega) = \tilde{f}\big(\sqrt{2b(x-x_0)}/\sigma,\omega\big)e^{-b(x-x_0)^2/2\sigma^2}$ represents a solution to:

$$j\omega f(x,\omega) + \hat{L}_x f(x,\omega) = 0, \tag{5.66}$$

with $\hat{L}_x$ defined by Eq. (5.58). Let f_1 and f_2 be the solutions of Eq. (5.66) corresponding to the parabolic cylinder functions that vanish at $+\infty$ and $-\infty$,

respectively. The solution of problem (5.52) on each graph edge can be expressed as a linear combination of these functions:

$$G^0((i_1,i_2,x),\omega) = \lambda_1(i_1,i_2,\omega)f_1(x,\omega) + \lambda_2(i_1,i_2,\omega)f_2(x,\omega) \tag{5.67}$$

The coefficients $\lambda_1(i_1,i_2,\omega)$ and $\lambda_2(i_1,i_2,\omega)$ corresponding to each edge are found (for a given frequency) by matching the inhomogeneous "vertex" boundary conditions of the problem (5.52) (for that frequency). Thus, the analytical expression for the solution of the problem (5.52) can be expressed in terms of parabolic cylinder functions. Besides the importance in its own right, the described analytical approach can be used for the testing of the accuracy of numerical techniques.

Step 3

Using observation (3) from the previous section, the cross-spectral density $S_{\beta\alpha}(\omega)$ can be expressed as:

$$S_{\beta\alpha}(\omega) = -\frac{2}{\omega}\mathrm{Im}\left\{\int_{-\infty}^{\infty}\frac{\sigma^2}{2}\frac{\partial^2}{\partial x^2}\left(\sum_{i_\alpha,i_\beta} i_\beta G^0\right) - b\frac{\partial}{\partial x}\left((x-x_0)\sum_{i_\alpha,i_\beta} i_\beta G^0\right)dx\right\} \tag{5.68}$$

The derivatives in (5.68) can be integrated and appropriate vertex boundary conditions can be used for simplification. By using formulas (5.52) and (5.61–5.66), one can derive the following formula for the cross-spectral density, for $\alpha<\beta$:

$$S_{\beta\alpha}(\omega) = \frac{4\sigma\sqrt{b}}{\omega^2\sqrt{\pi}\int_{-\beta}^{\beta} e^{b(y-x_0)^2/\sigma^2}dy} - \frac{2\sigma^2}{\omega}\mathrm{Im}\left[\frac{\partial G^0}{\partial x}\left(1,-\beta^+,\omega\right) - \frac{\partial G^0}{\partial x}\left(1,\beta^-,\omega\right) + \frac{\partial G^0}{\partial x}\left(\beta^+,\omega\right)\right], \tag{5.69}$$

while for $\alpha > \beta$ we have:

$$S_{\beta\alpha}(\omega) = \frac{4\sigma\sqrt{b}}{\omega^2\sqrt{\pi}\int_{-\alpha}^{\alpha} e^{b(y-x_0)^2/\sigma^2}dy} - \frac{2\sigma^2}{\omega}\mathrm{Im}\left\{\sum_{i_\alpha}\left[\frac{\partial G^0}{\partial x}\left(1,i_\alpha,-\beta^+,\omega\right) - \frac{\partial G^0}{\partial x}\left(1,i_\alpha,\beta^-,\omega\right)\right] + \frac{\partial G^0}{\partial x}\left(\beta^+,\omega\right)\right\}. \tag{5.70}$$

According to Eq. (5.67), $G^0(\mathbf{y},\omega)$ can be represented in terms of parabolic cylinder functions on each graph edge, hence explicit analytical formula in terms of parabolic cylinder functions can be given for cross-spectral density $S_{\beta\alpha}(\omega)$.

Results of the calculations for the cross-spectral density $S_{\beta\alpha}(\omega)$ using formulas (5.69) and (5.70) are presented in Fig. 5.10 where OU input process with $b=\sigma=1$ and $x_0=x_s=0$ has been considered.

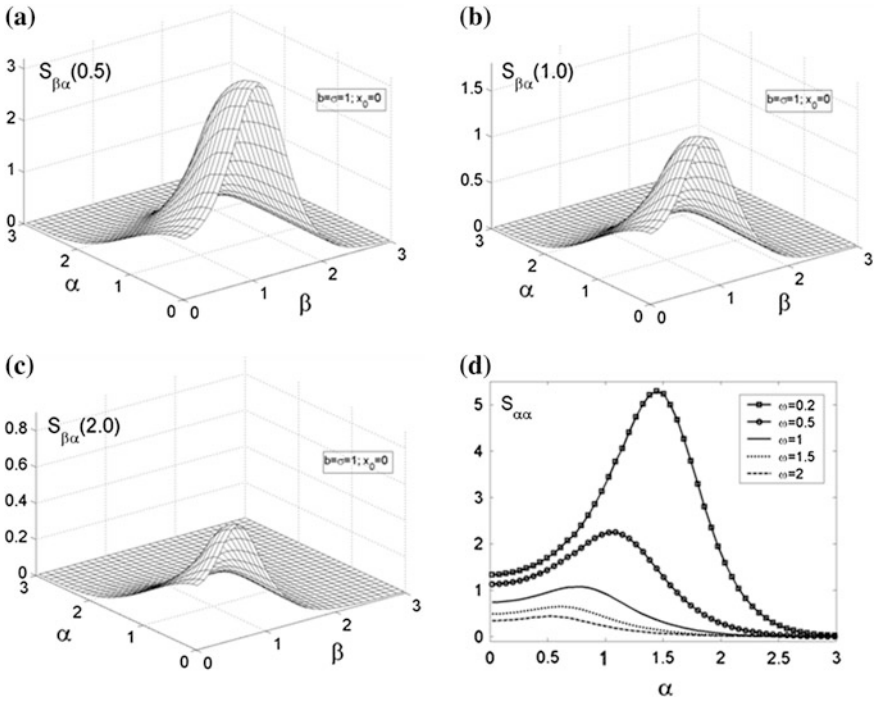

Fig. 5.10 Variation of cross spectral density $S_{\beta\alpha}$ with respects to the widths β and α of the two loops, for $\omega = 0.5$ (**a**), 1 (**b**), 2 (**c**); (**d**) Diagonal sections $S_{\alpha\alpha}$ are plotted for different frequencies f ($\omega = 2\pi f$). (© 2004 APS, [6])

Variations of the cross-spectral density $S_{\beta\alpha}(\omega)$ with respect to the widths β and α of the two loops are presented in Fig. 5.10a–c for selected values of the frequency while their diagonal sections ($S_{\alpha\alpha}(\omega)$) are compared in Fig. 5.10d for a better understanding of the relation between them. The cross-spectral density has negligible values outside of a finite region around the origin and this region becomes smaller when the frequency is increased. It can be clearly observed that the maximum of $S_{\alpha\alpha}(\omega)$ becomes more pronounced and it is shifted towards "wider loops" as the frequency is decreased. This suggests that two Preisach systems whose Preisach distributions coincide near the origin, should have approximately the same spectral noise densities for high frequencies. The computational results feature monotonic variations of $S_{\beta\alpha}(\omega)$ with respect to ω for fixed β and α, which leads to the conclusion that the spectral noise density $S_Y(\omega)$ of a Preisach system should be a decreasing function of frequency, regardless of the shape of the Preisach distribution. It is also expected that $S_{\beta\alpha}(\omega)$ is decreased for every β and α as x_0 is shifted from zero.

Step 4

Using formulas (5.69) and (5.70) for cross-spectral densities $S_{\beta\alpha}(\omega)$ in Eq. (5.35), the spectral density for the output process of a Preisach system

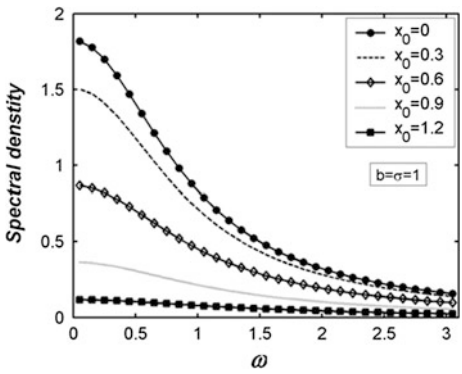

Fig. 5.11 Spectral density S_Y for a hysteretic system with uniform Preisach distribution for different values of input average value x_0 ($b = \sigma = 1$). (© 2004 APS, [6])

characterized by distribution μ and driven by an OU process can be found. Results of the calculations for the spectral density $S_Y(\omega)$ of a Preisach system with uniform distribution, $\mu(\alpha) = 1$, $\alpha \in (0, 1)$, are presented in Fig. 5.11.

As a final remark let us mention that in the limit of $b \to \infty$ with σ/b maintained constant, the Ornstein-Uhlenbeck process converges to a white noise process. Consequently, the output spectral density for the white noise input can be obtained either directly or as a limit of the result obtained for the Ornstein-Uhlenbeck process. In Refs. [18–20], Radons derived directly the output spectral density for a white noise input using a different technique and proved that long-time tails and even $1/f$ noise are quite general features of the class of symmetric Preisach models driven by uncorrelated noise.

5.3 Numerical Approach to Noise Spectral Analysis in Hysteretic Systems

For the numerical calculation of the output spectral density, a sufficiently large number of realizations of the noise input are generated according to the technique presented in Chap. 2 for the specific class of noise given in the problem. Then, the Fast-Fourier-Transform (FFT) technique is used to evaluate the spectral density of each output signal and average the output spectra to obtain their expected values. The power spectral density of the output signal is computed as:

$$S_Y(\omega) = \lim_{T\to\infty} \frac{E\left\{|Y_T(\omega)|^2\right\}}{2T} \tag{5.71}$$

where $Y_T(\omega) = \int_{-T}^{T} y(t)e^{-j\omega t}dt$ is the "truncated" Fourier transform of the output signal $y(t)$. This approach has been implemented numerically in HysterSoft© and used to compute the noise spectral densities of the output signal for various hysteretic systems. For the simulations presented in this chapter, the spectrum of the output signal has been computed by averaging over 500 statistical (Monte-Carlo)

simulations, which provided a very good accuracy of the results. The total time to evaluate $S_Y(\omega)$ on a one-processor computer operating at 3 GHz is less than a second for the energetic and Jiles-Atherton Models and less than a minute for the Preisach Model. The reliability of this numerical approach was successfully tested against several analytical results provided in the previous section (Sect. 5.1) for the hard limiter system, the hysteretic rectangular loop, and symmetric Preisach systems.

In this section, sample of the simulation results obtained using various hysteresis models driven by OU noise inputs are presented and analyzed. In the case of energetic, Jiles-Atherton, Preisach and Coleman-Hodgdon models, the parameters are chosen such that the corresponding major hysteretic loops have the same coercive input $x_c = 1.28$, output saturation $y_{sat} = 7.7 \times 10^5$, and output remanence $y_R = 4 \times 10^5$. These values, measured in A/m, characterize the major hysteretic loop of a permalloy ferrite [21]. The rest of models parameters and simulation are given in the subsections dedicated to a specific model. As discussed in the final subsections, the intrinsic differences between the algebraic, differential, and integral modeling of hysteresis are well exposed when the systems are driven by noisy inputs and their stochastic behaviors are compared against each other [22].

This analysis can be extended to the noise model of interest to the reader by selecting the noise model in HysterSoft© and running associated simulations.

5.3.1 Preisach Model

The Preisach distribution was identified on a discrete mesh of points using a set of first-order reversal-curves and employing Eqs. (1.17) and (1.18). This discrete distribution was then fitted to a 2-D normal distribution in order to speed up the computations:

$$P(\alpha,\beta) = \frac{y_{sat}S}{2\pi\, H_{\sigma i}H_{\sigma c}} \cdot \exp\left[-\frac{(\alpha+\beta-2H_0)^2}{4H_{\sigma i}^2} - \frac{(\alpha-\beta)^2}{4H_{\sigma c}^2}\right], \tag{5.72}$$

where $S = 0.88$, $H_{\sigma i} = 2.23$ A/m, $H_{\sigma c} = 0.49$ A/m, and the average value of the critical fields of the particles was found to be $H_0 = 1.9$ A/m. The reversible component of the Preisach distribution was also approximated by a normal distribution:

$$R(\alpha) = \frac{y_{sat}(1-S)}{\sqrt{2\pi}\, H_{\sigma r}} \cdot \exp\left(-\frac{\alpha^2}{4H_{\sigma r}^2}\right), \tag{5.73}$$

where $H_{\sigma r} = 2.12$. The initial hysteretic state in all simulations was assumed the zero-field anhysteretic curve (also known as the a.c. demagnetized state magnetism). In Fig. 5.12 the major hysteresis curve and an output realization of this Preisach system driven by an OU input are presented. The output spectra for different values of the noise strength are plotted in Fig. 5.13.

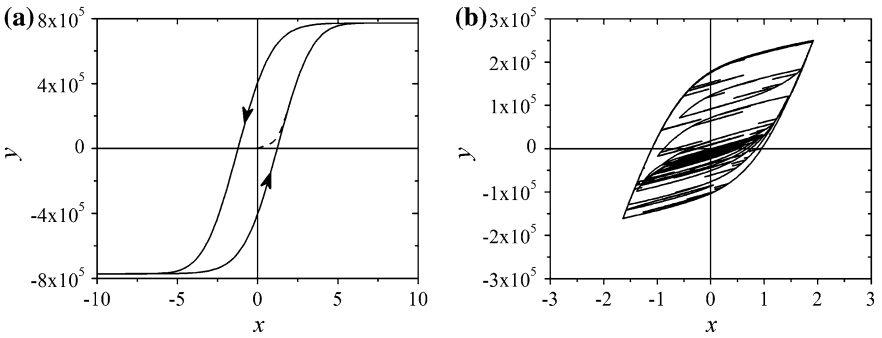

Fig. 5.12 Major hysteresis loop (**a**) and Minor hysteresis loops driven by an noisy input having an Ornstein-Uhlenbeck distribution with $b = \sigma = 1$ (**b**)

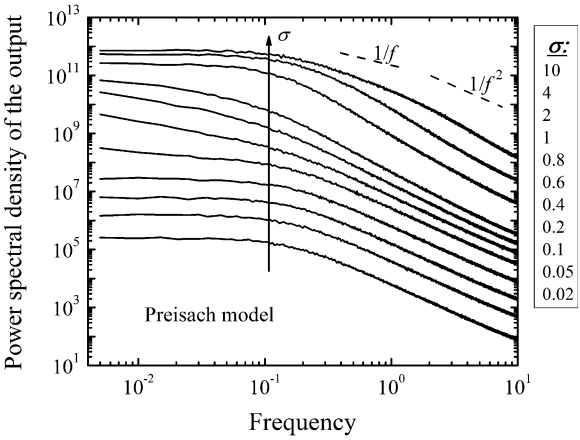

Fig. 5.13 Spectral density of the output of Preisach Model for different values of noise strength σ

5.3.2 Energetic Model

The parameters of the EM have been identified by using the technique presented in Sect. 1.4.3: $h = 0.4$, $k = 1.2$, $g = 8.24$, $c_r = 0.02$, $q = 10$, and $N_e = 3.5 \times 10^{-7}$. In Fig. 5.14 the major hysteresis curve and an output realization of this EM driven by an OU input are presented. The output spectra are plotted in Fig. 5.15 for different values of the noise strength.

5.3.3 Jiles-Atherton Model

The parameters of the JAM used in the simulations presented in this section are $k = 2.44$, $a = 4.36$, $\alpha = 1.7 \times 10^{-5}$, and $c = 0.49$ In Fig. 5.16 the major hysteresis

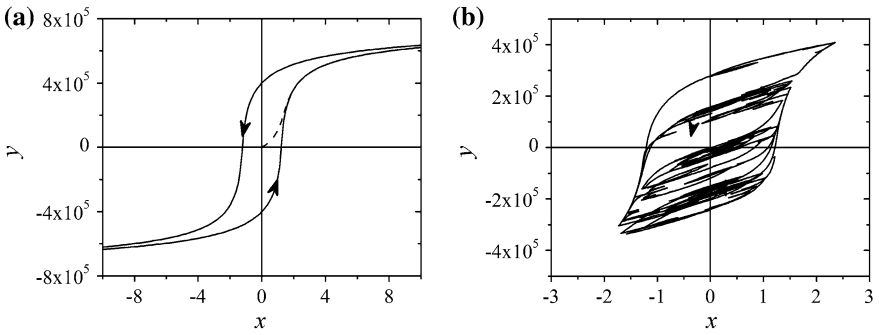

Fig. 5.14 Major hysteresis loop (**a**) and minor hysteresis loops driven by an noisy input having an Ornstein-Uhlenbeck distribution with $b = \sigma = 1$ (**b**)

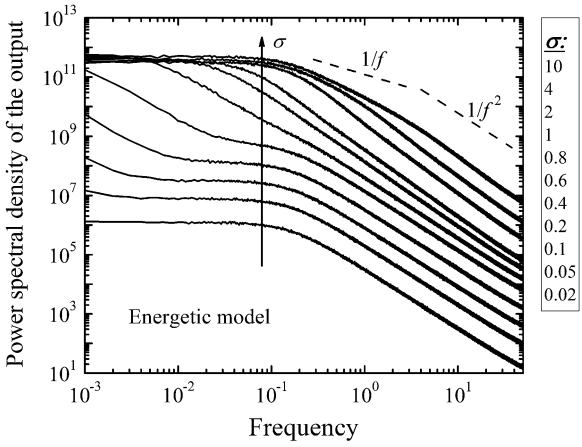

Fig. 5.15 Spectral density of the output of energetic model for different values of noise strength σ

curve and an output realization of this JAM driven by an OU input are presented. The output spectra for different values of the noise strength are plotted in Fig. 5.17.

Figures 5.13, 5.15, and 5.17 show the results of the power spectral density of the magnetization computed by using the EM, JAM, and the PM, respectively, for different values of the diffusion coefficient (or noise strength) σ ranging from 40 for the top-most curves to 0.02 for the bottom-most curves. Let us remind that the spectrum of the magnetic field (noise input) has a Lorentzian-shape, which is flat in the low-frequency region and has $1/f^2$ decay for high-frequency region. As observed from these figures the last property is transferred by the hysteretic systems and the output spectra features a $1/f^2$ at high frequency region. It is interesting to note that all models predict a flat spectrum at low frequencies and large magnitudes of the input signal (large values of σ) and an increase of the low-frequency components for values of σ slightly lower than the coercive input, x_c. As opposed to the PM and EM, the JAM also predicts an increase in the power spectra

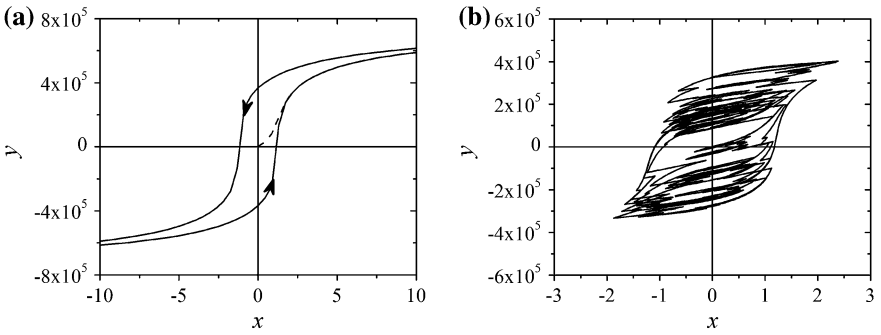

Fig. 5.16 Major hysteresis loop (**a**) and minor hysteresis loops driven by an noisy input having an Ornstein-Uhlenbeck distribution with $b = \sigma = 1$ (**b**)

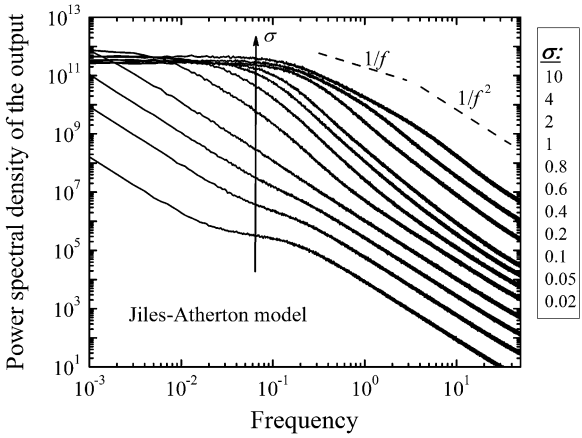

Fig. 5.17 Spectral density of the output of Jiles-Atherton Model for different values of the noise strength σ

at low frequencies even for relatively low values of σ. In general, the hysteretic systems with OU input presented monotonic spectral densities and the increase in the input average x_o resulted in the decrease in the output noise.

5.3.4 Coleman-Hodgdon Model

The reverse Coleman-Hodgdon model with (1.117) with the material functions given by (1.127) and (1.128) is used below. The model parameters were identified as $A_1 = 1$, $A_2 = 2 \times 10^{-6}$, $A_3 = -0.7$, $A_4 = 0.01$, $\alpha = 8 \times 10^{-7}$, $x_{cl} = 2.5$, and $y_{cl} = 3 \times 10^6$. In Fig. 5.18 the major hysteresis curve and an output realization of this Coleman-Hodgdon system driven by an OU input are presented. The output spectra are plotted in Fig. 5.19 for different values of the noise strength.

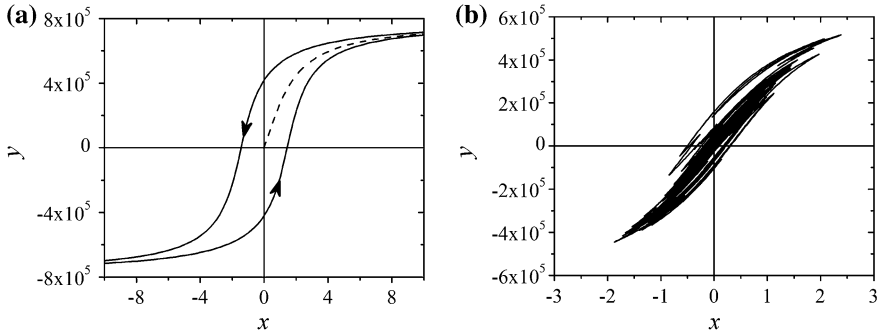

Fig. 5.18 Major hysteresis loop (**a**) and minor hysteresis loops driven by a noisy input having an Ornstein-Uhlenbeck distribution with $b = \sigma = 1$ (**b**)

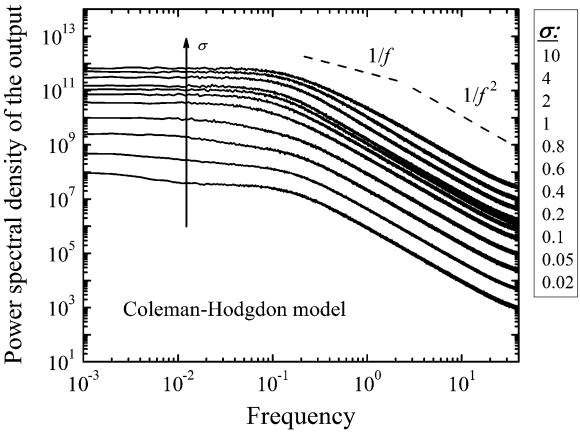

Fig. 5.19 Spectral density of the output of Coleman-Hodgdon model for different values of the noise strength σ

5.3.5 *Bouc-Wen Model*

Three sets of parameters have been used in the case of the Bouc-Wen model:

Set 1: $A = 2$, $\alpha = 0$, $\beta = 0.5$, $D = 2$, $\gamma = 0.1$, $k = 1$, $n = 1$;
Set 2: $A = 2$, $\alpha = 0$, $\beta = 0.5$, $D = 1$, $\gamma = 0.1$, $k = 1$, $n = 4$;
Set 3: $A = 2$, $\alpha = 0.7$, $\beta = 0.5$, $D = 1$, $\gamma = 0.1$, $k = 1$, $n = 1.1$.

These parameters correspond to hysteresis loops that resemble the stop operator often used in elasticity and plasticity (Figs. 5.20, 5.21, 5.22 and 5.23). Figures 5.20, 5.21, and 5.22 present the major hysteresis curves and the output realization for the Bouc-Wen model with the parameters given above. The output spectra are plotted in Fig. 5.15 for different values of the noise strength.

In conclusion, the numerical approach used here provides a relatively fast and reliable way to analyze the power spectral densities of complex hysteretic systems.

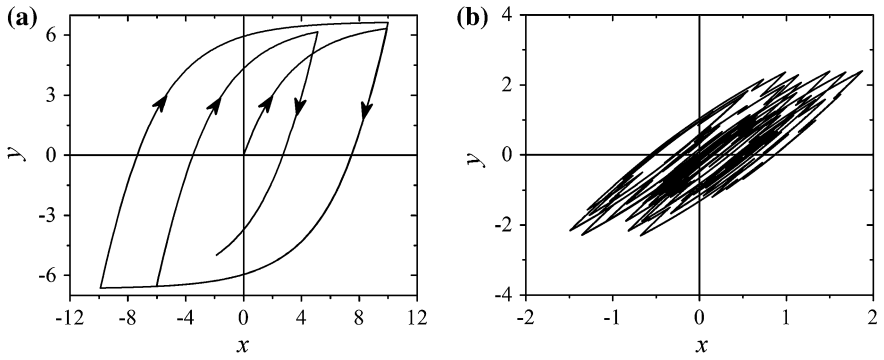

Fig. 5.20 Hysteresis loops driven by a deterministic input with simple monotonic variation (**a**) and a noisy input having an Ornstein-Uhlenbeck distribution with $b = \sigma = 1$ (**b**) the parameters of the Bouc-Wen model are defined in Set 1

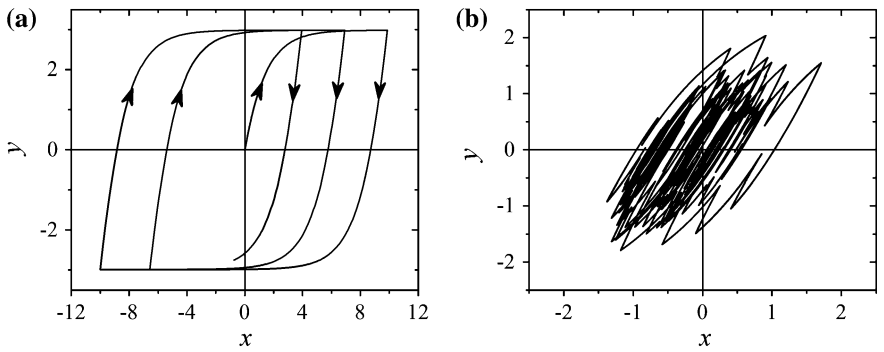

Fig. 5.21 Hysteresis loops driven by a deterministic input with simple monotonic variation (**a**) and a noisy input having an Ornstein-Uhlenbeck distribution with $b = \sigma = 1$ (**b**) the parameters of the Bouc-Wen model are defined in Set 2

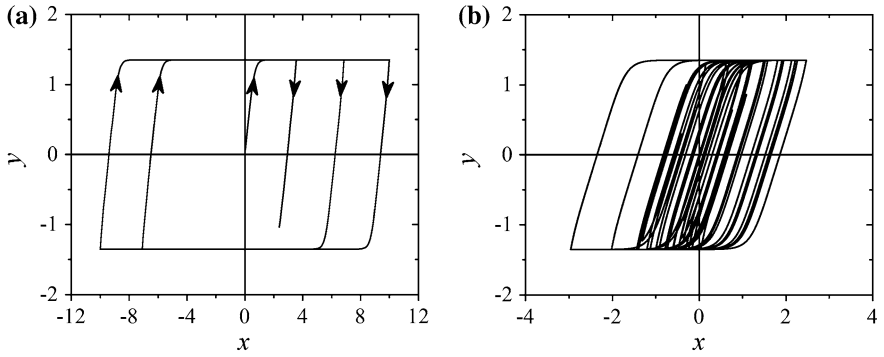

Fig. 5.22 Hysteresis loops driven by a deterministic input with simple monotonic variation (**a**) and a noisy input having an Ornstein-Uhlenbeck distribution with $b = \sigma = 1$ (**b**) the parameters of the Bouc-Wen model are defined in Set 3

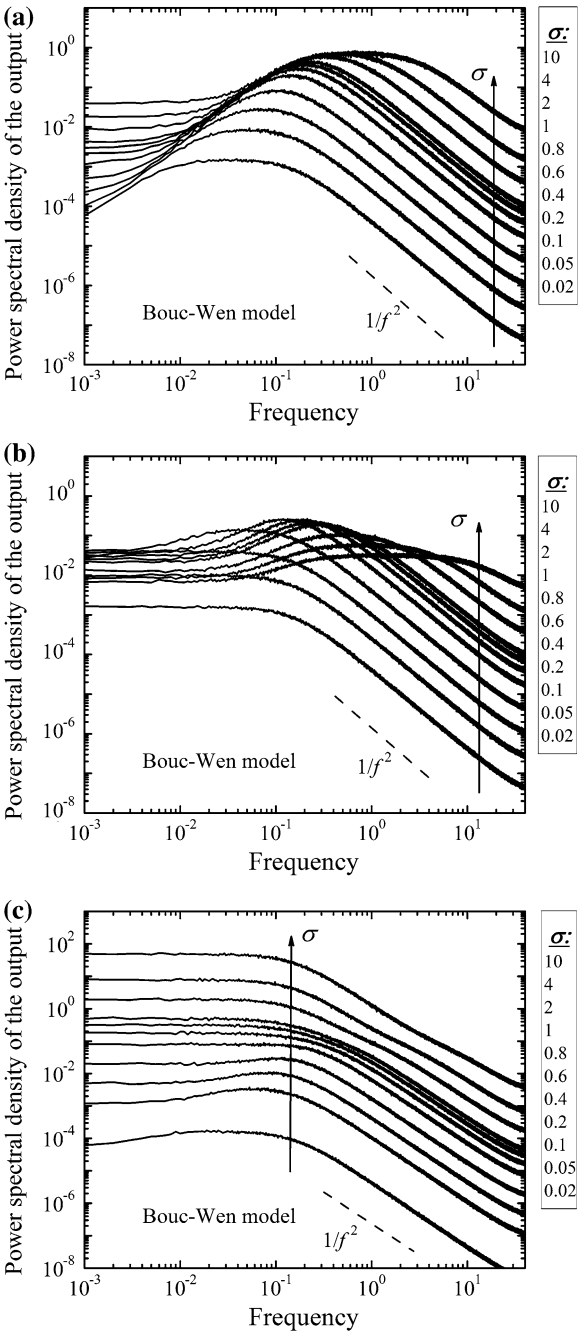

Fig. 5.23 Spectral densities of the output of Bouc-Wen model for different values of the noise strength σ in the case of the model parameters defined by Set 1 (**a**), Set 2 (**b**), and Set 3 (**c**)

According to our analysis, the output spectra deviate significantly from the Lorentzian shape of the input process for values of the diffusion coefficient near and smaller than the coercive field. The intrinsic differences between the transcendental, differential, and integral modeling of hysteresis yield significantly different spectra at low frequency region, which reflect the diverse long-time correlation behavior. It is also apparent from this study that the spectral analysis is a powerful characterization tool that can be used to design filters based on hysteretic systems.

References

1. Gardiner, C. (2009). *Stochastic methods: A handbook for the natural and social sciences*. Berlin: Springer.
2. Freidlin, M. I., & Wentzell, A. D. (1993). Diffusion processes on graphs and the averaging principle. *Annals of Probability, 21*(4), 2215–2245.
3. Freidlin, M. I. (1996). *Markov processes and differential equations: Asymptotic problems*. Berlin: Springer.
4. Freidlin, M. I., Mayergoyz, I. D., & Pfeiffer, R. (2000). Noise in hysteretic systems and stochastic processes on graphs. *Physical Review E, 62*, 1850–1856.
5. Mayergoyz, I., & Dimian, M. (2003). Analysis of spectral noise density of hysteretic systems driven by stochastic processes. *Journal of Applied Physics, 93*(10), 6826–6828.
6. Dimian, M., & Mayergoyz, I. D. (2004). Spectral density analysis of nonlinear hysteretic systems. *Physical Review E*, *70*, Article 046124.
7. Dimian, M. (2008). Extracting energy from noise: noise benefits in hysteretic systems. *NANO*: *Brief reviews and reports*, *3*(5), 391–397.
8. Dimian, M., Gîndulescu, A., & Andrei, P. (2010). Influence of noise temporal correlation on magnetization spectra and thermal relaxations in soft magnetic materials. *IEEE Transactions on Magnetics, 46*(2), 266–269.
9. Mayergoyz, I. D. (2003). *Mathematical models of hysteresis and their applications* (2nd ed.). New York: Academic Press.
10. Melnikov, V. I. (1993). Schmitt trigger: A solvable model of stochastic resonance. *Physical Review E, 48*(4), 2481–2489.
11. Lindner, B., Garcia-Ojalvo, J., Neiman, A., & Schimansky-Geier, L. (2004). Effects of noise in excitable systems. *Physics Reports*, *392*, 321–424.
12. Abramowitz, M., & Stegun, I. (Eds.). (1972). *Handbook of mathematical functions*. New York: Dover Publications.
13. Papoulis, A. (2002). *Probability, random variables and stochastic processes*. New York: McGraw-Hill.
14. van Vleck, J. H. (1943). The spectrum of clipped noise. *RRL Report* 51.
15. Pikovsky, A. S., & Kurths, J. (1997). Coherence resonance in a noise-driven excitable system. *Physical Review Letters, 78*, 775–778.
16. Korman, C. E., & Mayergoyz, I. D. (1996). Semiconductor noise in the framework of semiclassical transport. *Physical Review B, 54*, 17620–17627.
17. Berezin, I. S., & Zhidkov, N. P. (1965). *Computing methods*. London: Pergamon.
18. Radons, G. (2008). Hysteresis-induced long-time tails. *Physical Review Letters*, *100*, Article 240602.
19. Radons, G. (2008). Spectral properties of the Preisach hysteresis model with random input. I. General results. *Physical Review E*, *77*, Article 061133.
20. Radons, G. (2008). Spectral properties of the Preisach hysteresis model with random input. II. Universality classes for symmetric elementary loops. *Physical Review E*, *77*, Article 061134.

21. Andrei, P., & Adedoyin, A. (2009). Noniterative parameter identification technique for the energetic model of hysteresis. *Journal of Applied Physics*, *105*, Article 07D523.
22. Adedoyin, A., Dimian, M., & Andrei, P. (2009). Analysis of noise spectral density for phenomenological models of hysteresis. *IEEE Transactions on Magnetics*, *45*(10), 3934–3937.